Sustainable Energy & Fuels

ROYAL SOCIETY OF CHEMISTRY

PAPER

View Article Online
View Journal | View Issue

Cite this: *Sustainable Energy Fuels*, 2026, **10**, 1282

Cobalt manganese sulfide nanosheets: a robust bifunctional catalyst for alkaline water electrolysis

Harshini Sharan, [a] Angappan Kausalya,[b] Senthilkumar Lakshmipathi, [b] Pavithra Karthikesan,[a] Jayachandran Madhavan [a] and Alagiri Mani *[a]

Received 26th September 2025
Accepted 23rd January 2026

DOI: 10.1039/d5se01288k

rsc.li/sustainable-energy

Designing efficient and robust bifunctional electrocatalysts for overall water splitting (OWS) is crucial for advancing sustainable energy technologies. Nanosheet (NS)-like cobalt manganese sulfide (COMS) was synthesized *in situ* on nickel foam (NF) *via* a one-step hydrothermal method. The binder-free COMS NSs on NF electrocatalyst demonstrated low overpotentials of 197 mV and 270 mV for the hydrogen evolution reaction (HER) and the oxygen evolution reaction (OER), respectively, to achieve a current density of 10 mA cm^{-2} in 1 M KOH. The electrocatalyst facilitated a low overall cell potential of 1.54 V to attain 10 mA cm^{-2} current density, when utilized as both anode and cathode. COMS NSs on NF exhibited exceptional durability, ensuring stable operation over 300 h of continuous testing. The robustness of the electrocatalyst after long-term operation was examined with the aid of post-stability analysis. Additionally, density functional theory (DFT) was conducted to corroborate the experimental findings. All these outcomes emphasize that COMS NSs on NF are a highly promising earth-abundant electrocatalyst for alkaline water splitting.

1 Introduction

The ever-growing need for energy due to rapid industrialization, rising global population, and the critical need to combat climate change is causing immense changes in the world's energy ecosystem. Despite their long-standing dominance, traditional fossil fuel-based resources remain the main source of greenhouse gas emissions, which exacerbate environmental degradation and accelerate global warming. Therefore, clean and sustainable energy alternatives are needed to provide reliable energy and environmental protection.[1] Amidst an array of renewable choices, there is tremendous potential for electrochemical water splitting to act as a green energy and environmental solution. A major obstacle to its success lies in finding efficient electrocatalysts for the hydrogen evolution reaction (HER) and the oxygen evolution reaction (OER) under alkaline conditions. When it comes to electrolytes, an alkaline medium is preferred for overall water splitting. This is because the ionic conductivity of alkaline electrolytes is high, which is advantageous for the rapid movement of ions. Also, the preparation of alkaline electrolytes is facile, consisting of simply dissolving the base in water. In addition, these conditions are more cost-effective than acidic ones, and therefore, they are suitable for use in large-scale applications.[2,3] The current benchmarks for HER and OER are materials based on Pt and Ir/Ru, but their high costs prevent them from being widely used.[4] This has prompted extensive research into alternative transition-metal-based catalysts such as oxides,[5–8] nitrides,[9–13] phosphides,[14–17] and chalcogenides,[18–25] which exhibit diverse structures and excellent catalytic activity.

Hybrid materials based on transition metal sulfides have garnered significant attention as emerging electrocatalysts for the HER and OER. Their appeal lies in their cost-effectiveness, high catalytic activity, diverse redox reactions, enhanced electrical conductivity, and the flexibility provided by sulfur, which facilitates improved electron transfer.[26] Fascinatingly, their structure features covalently constrained layers of metal atoms, with weak van der Waals forces enabling interactions between distinct layers, thereby opening up a novel avenue for energy storage and conversion applications.[27,28] For instance, Qiang *et al.* reported Fe-doped CoS_2 nanorods *via* a hydrothermal approach, and they presented an overall cell voltage of 1.62 V at 10 mA cm^{-2} current density with excellent durability as an efficient bifunctional electrocatalyst.[29] Huang *et al.* demonstrated Co_3S_4/NiS_2 heterostructures achieving a low cell potential of 1.59 V to reach 10 mA cm^{-2}, with stable operation for 24 h in 1 M KOH.[30] Dhakal *et al.* hybridised $CoMnS_2$ with Fe-doped (1T)-phase VS_2 core–shell nanorod clusters on Ni foam, which required 1.51 V at 10 mA cm^{-2} current density and was stable for approximately 40 h.[31]

Building on the concepts of the previously mentioned reports, the ternary cobalt manganese sulfide (COMS) system offers several advantages over its binary counterparts. The electrochemical features are strengthened, which contribute to

[a]*Department of Physics and Nanotechnology, SRM Institute of Science and Technology, Kattankulathur, Chengalpattu 603203, India. E-mail: alagirim@srmist.edu.in*
[b]*Department of Physics, Bharathiar University, Coimbatore 641046, India*

greater HER and OER activity with less overpotentials and retention rates, when multi-component metal sulfides are combined.[26] In addition, there have been many attempts to explore binary, ternary, and quaternary transition-metal-based chalcogenides as an alternative to replace noble-metal-based electrocatalysts. Theoretical and experimental findings have shown that ternary metal sulfides are the most effective electrocatalysts, suggesting that these compounds are the best choice for optimizing the electronic states.[32,33]

Herein, we have synthesized COMS nanosheets (NSs) grown *in situ* on Ni foam *via* a simple and cost-effective hydrothermal approach. The resultant electrocatalyst was subjected to structural, morphological, and compositional analysis, followed by electrochemical measurements for the HER and OER. As anticipated, excellent HER and OER electrocatalytic activity with outstanding stability for pristine COMS NSs in 1 M KOH was observed. Additionally, as a symmetric electrode in a water electrolyzer, it unveiled a low cell voltage of 1.54 V to attain 10 mA cm^{-2} current density with exceptional long-term stability.

2 Experimental section

2.1. Materials

The following analytical grade chemicals were obtained from Sigma-Aldrich: cobalt(II) nitrate hexahydrate, manganese(II) nitrate tetrahydrate, and thiourea. Ni foam (NF) was procured from Vritra Technologies (Delhi, India), and KOH pellets were purchased from SRL, Chennai.

2.2. Preparation of COMS NSs on NF

To synthesize COMS NSs, a 2 × 4 cm^2 piece of nickel foam (NF) was pre-treated with 3 M HCl, ethanol, and deionized (DI) water to remove any surface contaminants and oxide layers. Precursors of 0.1 M of $Co(NO_3)_2 \cdot 6H_2O$, 0.1 M of $Mn(NO_3)_2 \cdot 4H_2O$, and 0.2 M of CH_4N_2S (thiourea) were optimally weighed and dissolved in 50 mL of DI water. The mixture was stirred for 1 h to obtain a homogeneous solution. After that, the obtained solution was poured into an autoclave containing pre-treated NF positioned at a 45° angle. At 120 °C for 15 h, the hydrothermal reaction occurred. Upon cooling, the sample was extensively washed with DI water and ethanol, allowed to dry overnight, and then subjected to further characterization. A schematic representation for the synthesis of the COMS NS electrocatalyst, followed by electrochemical measurements, is illustrated in Fig. 1.

2.3. Characterizations

The produced electrocatalyst's morphology and physical characteristics were examined using a variety of characterizations. The formation and the phase purity of the resultant catalyst were examined using an X-ray diffractometer (XRD, PANalytical instrument with Cu Kα radiation (1.54 Å)). Additionally, the morphology and the elemental distribution of the electrocatalyst were studied by high-resolution transmission electron microscopy (HR-TEM, JEOL, Japan, JEM-2100 plus) and high-resolution scanning electron microscopy (HR-SEM, Thermoscientific Apreo S). Bruker Alpha-T equipment was used to acquire the Fourier transform infrared (FT-IR) spectrum for the functional group analysis. The catalyst's surface area was measured using a Quanta Chrome/Autosorb IQ instrument, which produces Brunauer–Emmett–Teller (BET) isotherms. With the use of X-ray photoelectron spectroscopy (XPS, Phi Versa probe-3), the oxidation state and elemental makeup of the catalysts were investigated.

2.4. Electrochemical measurements

Utilising an Origalys electrochemical workstation, the electrocatalytic water-splitting analysis of COMS NSs was assessed. All electrochemical measurements were conducted at room temperature in 1 M KOH electrolyte using a standard three-

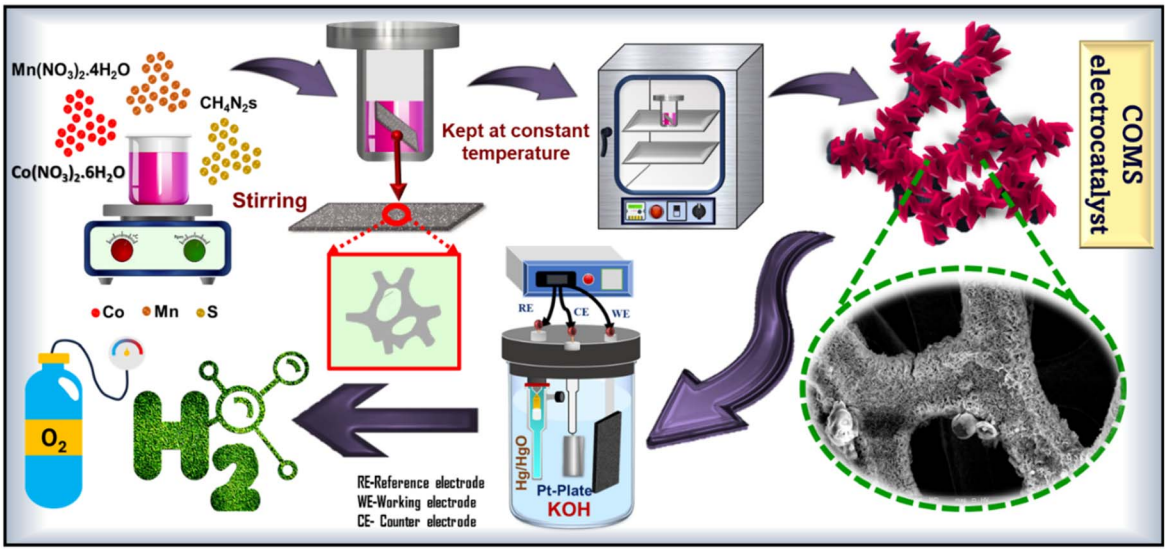

Fig. 1 Schematic representation for the synthesis of the COMS NS electrocatalyst *via* the hydrothermal method, followed by electrochemical measurements.

electrode configuration. This configuration included a platinum plate as the counter electrode, Hg/HgO with 1 M KOH as the reference electrode, and COMS NSs as the working electrode. Initially, cyclic voltammetry (CV) was conducted at a 40 mV s^{-1} scan rate for 40 consecutive cycles to ensure current stability. A steady-state polarisation curve was subsequently obtained by conducting linear sweep voltammetry (LSV). Eqn (1) was employed to convert all potentials measured against the Hg/HgO (E°(Hg/HgO) = 0.0983 V) reference electrode to the reversible hydrogen electrode (RHE) scale:

$$E(\mathrm{RHE}) = E(\mathrm{Hg/HgO}) + E^{\circ}(\mathrm{Hg/HgO}) + 0.059 \times \mathrm{pH}\ (\mathrm{V}) \quad (1)$$

The following expressions were employed to determine the overpotential (η) necessary for the HER and the OER:

$$\eta_{\mathrm{HER}} = 0 - E(\mathrm{RHE})\ (\mathrm{V}) \quad (2)$$

$$\eta_{\mathrm{OER}} = E(\mathrm{RHE}) - 1.23\ (\mathrm{V}) \quad (3)$$

The Tafel equation was employed to extract the Tafel slope from the linear region of the LSV plots, which provides insight into the reaction kinetics:

$$\eta_{(\mathrm{HER/OER})} = b \log j + a\ (\mathrm{mV\ dec^{-1}}) \quad (4)$$

where η denotes the overpotential, b denotes the Tafel slope, j denotes the current density, and a denotes a constant. The initial surge in the LSV curve was identified as the onset potential. The capacitive current obtained in the non-faradaic region at different scan rates was used to evaluate the electrochemically active surface area (ECSA). Electrochemical impedance spectroscopy (EIS) was executed between the frequency range 100 kHz to 10 mHz at a given perturbation potential. Chronoamperometric measurements were implemented to evaluate the electrocatalyst's long-term durability. Furthermore, the overall water-splitting process was examined using a two-electrode system that operated in a 1 M KOH solution for 300 hours, with identical COMS NS electrodes (COMS//COMS) functioning as both the cathode and anode.

2.5. Density functional theory (DFT)

Spin-polarized DFT calculations were carried out using the Vienna *Ab initio* Simulation Program (VASP).[34,35] To describe electronic interactions during structural optimization, the Perdew–Burke–Ernzerhof (PBE) exchange–correlation functional with generalized gradient approximation (GGA) was employed.[36] For all plane-wave basis sets, 500 eV was chosen as the cutoff energy. The Brillouin zone of CoMnS was sampled using a 3 × 3 × 1 Monkhorst–Pack *k*-mesh. For energy and force, the convergence criteria were set at 1×10^{-4} eV and 0.02 eV $Å^{-1}$. The DFT-D3 method was included to account for the weak van der Waals interactions in the system.[37] The optimized geometry, band structure, total density of states (TDOS), and partial density of states (PDOS) of the resultant electrocatalyst were theoretically discussed.

3 Results and discussion

The XRD analysis confirmed the formation of COMS NSs on Ni foam, which is shown in Fig. 2a. The peaks at 30.9°, 54.9°, and 92.6° correspond to the *hkl* planes of (002), (311), and (511) of CoS (PDF 03-065-0407), whereas the peaks positioned at 49.6°, 76.1°, and 98.2° resemble the *hkl* planes of (311), (422), and (600) of MnS_2 (PDF 00-010-0476), respectively. The highly intense Ni peaks (PDF 65-2865) located at 44.2°, 51.5°, and 76.1° corroborate with CoS, as well as MnS_2. Additionally, a minute peak at 37.6° corresponds to MnS (PDF 00-002-1268), the secondary phase formation. The less intense peak near 20° corresponds to NiS, which is due to the incorporation of nickel foam as a substrate.

FT-IR analysis is widely used to explore the functional groups and bonding nature of COMS NSs. Fig. 2b shows the FT-IR spectra of COMS NSs, which display distinct vibrational bands, with broad peaks above 3000 cm^{-1} that correspond to O–H stretching vibrations representing the existence of physically adsorbed water molecules attached to the transition metal sulfides (TMSs), and peaks at 2910 and 2973 cm^{-1} to C–H stretching modes.[38] Vibrational bands at 1682 and 1758 cm^{-1}

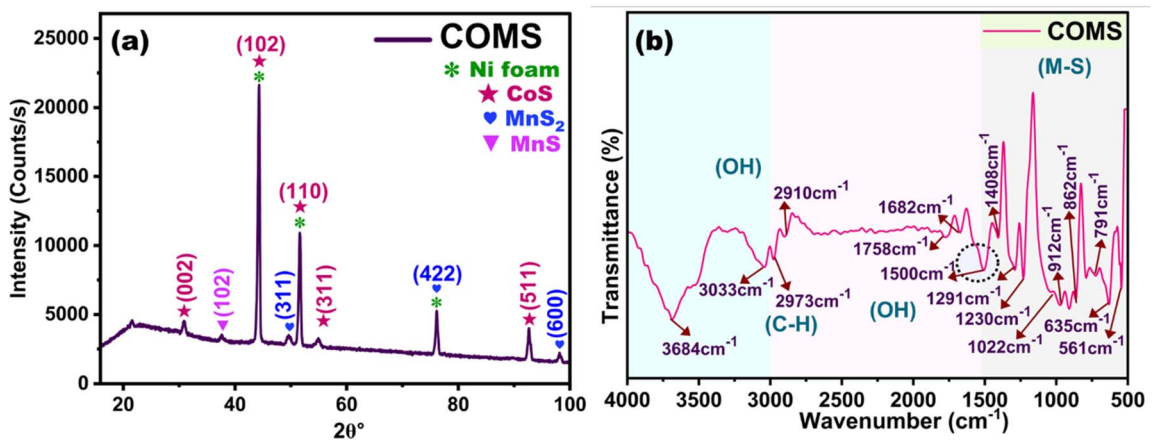

Fig. 2 (a) XRD pattern of the as-prepared COMS NSs grown *in situ* on NF. (b) The FT-IR spectrum highlighting the metal–sulfur bonding of the resultant electrocatalyst.

represent O–H bending, and peaks at 1200–1500 cm^{-1} could be C–O and C=C stretching vibrations. Interestingly, the sharp peaks at 912, 862, 791, 635, and 561 cm^{-1} are linked to Co–S and Mn–S stretching vibrations, proving that the bimetallic sulfide framework was successfully formed.[39,40]

The surface morphology and hierarchical architecture of the as-synthesized COMS NSs were thoroughly examined using HR-SEM, as shown in Fig. 3a–d. The low-magnification micrograph (Fig. 3a) reveals a uniformly coated network of nanostructures densely grown on the conductive substrate, indicating excellent nucleation and adhesion during synthesis. Upon closer observation at higher magnifications (Fig. 3b–d), the structures were found to consist of vertically aligned, ultrathin nanosheets (NSs) interwoven to form a loosely packed but continuous three-dimensional (3D) framework. The homogeneous distribution of the elements was confirmed through elemental mapping, as shown in Fig. 3e–h. These nanosheet-like structures, with their exposed edges, are particularly advantageous for electrocatalytic applications. The vertical alignment exposes a large number of active edge sites, while the inter-sheet voids facilitate efficient electrolyte infiltration and gas release, both critical for the HER and OER.[41–43]

This hierarchical growth suggests a self-assembly process driven by a synergistic interaction between cobalt, manganese, and sulfur precursors under the hydrothermal conditions. Such a textured morphology enhances not only the electrochemically active surface area (ECSA) but also promotes rapid charge transport pathways, contributing to increased catalytic efficiency and stability during water splitting. To gain deeper insights into the internal structure and crystallinity at the atomic scale, the obtained electrocatalyst, which was ultrasonically detached from the substrate, was subjected to HR-TEM, as depicted in Fig. 3i–k. The low-magnification TEM images (Fig. 3i and j) exhibit a wrinkled and layered nanosheet-like morphology, which is consistent with the SEM observations. The transparent regions confirm the ultrathin nature of the sheets, which are conducive to fast ion diffusion and electron transport during electrocatalysis.[44,45]

The HR-TEM image in Fig. 3k provides a closer view of the atomic lattice fringes, with distinct interplanar spacings of 1.61 Å, 1.01 Å, and 0.81 Å. These spacings are well indexed to the (311) and (422) planes of MnS_2, and the (102) and (110) planes of CoS, which are well correlated with the XRD results. Additionally, the SAED pattern (Fig. 3l) illustrates distinct concentric rings corresponding to the aforementioned planes, further confirming the polycrystalline nature of the COMS NSs. Hence, all these are expected to significantly contribute to better electrocatalytic performance.

To further understand the elemental oxidation states of the COMS NSs, XPS analysis was performed. Fig. 4a–d illustrates the XPS spectra of the obtained electrocatalyst. The survey spectrum (Fig. 4a) confirms the presence of Co, Mn, and S as key constituents, along with peaks of O and C. The high-resolution Co 2p spectrum (Fig. 4b) shows two main peaks at 781 eV and 796 eV corresponding to Co $2p_{3/2}$ and Co $2p_{1/2}$, respectively, along with distinct satellite features at 783 eV and 798 eV, which indicate the Co^{2+} oxidation state. Additionally, minor metallic cobalt peaks exist at the binding energies of 774 eV and 786 eV.[46,47]

The Mn 2p spectrum (Fig. 4c) exhibits three deconvoluted peaks corresponding to Mn $2p_{3/2}$ at the binding energies of 637 eV, 642 eV, and 645.2 eV, indicative of a mixed Mn^{2+}/Mn^{3+}

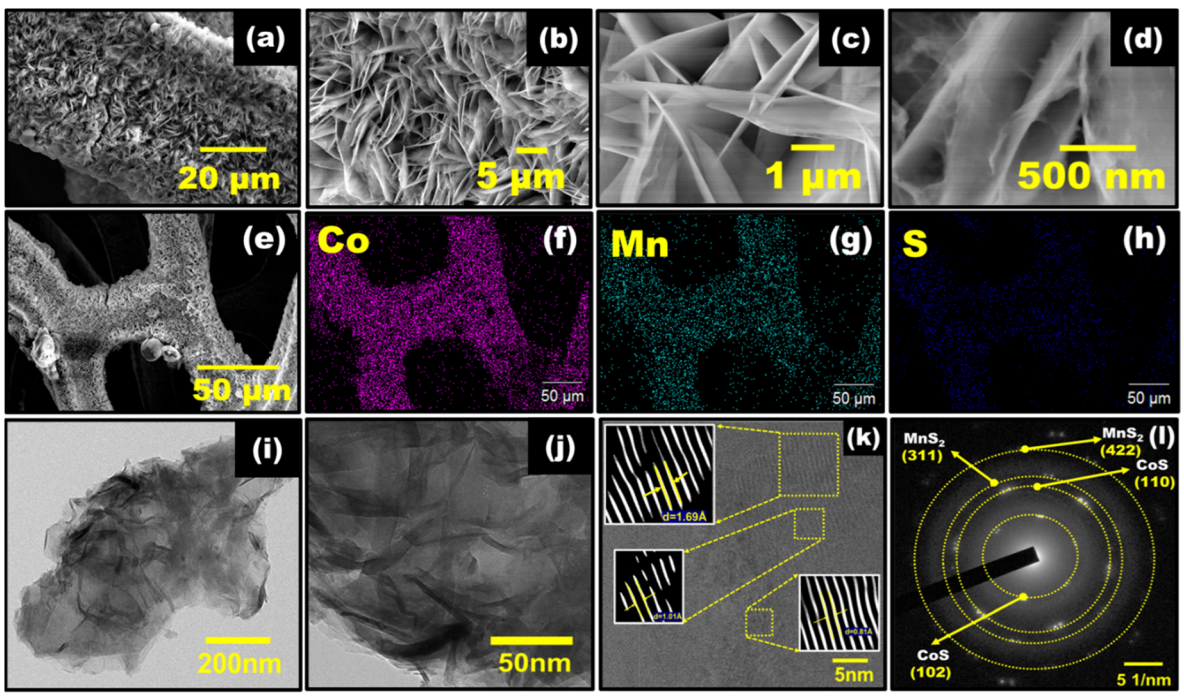

Fig. 3 (a–d) HR-SEM micrographs of COMS NSs on NF under different magnifications. (e–h) Elemental mapping of COMS NSs at 50 μm. (i–k) HR-TEM images of ultrathin nanosheet arrays with interplanar spacings (inset (k)-process FFT images). (l) The SAED pattern confirms the polycrystalline nature of the COMS NSs.

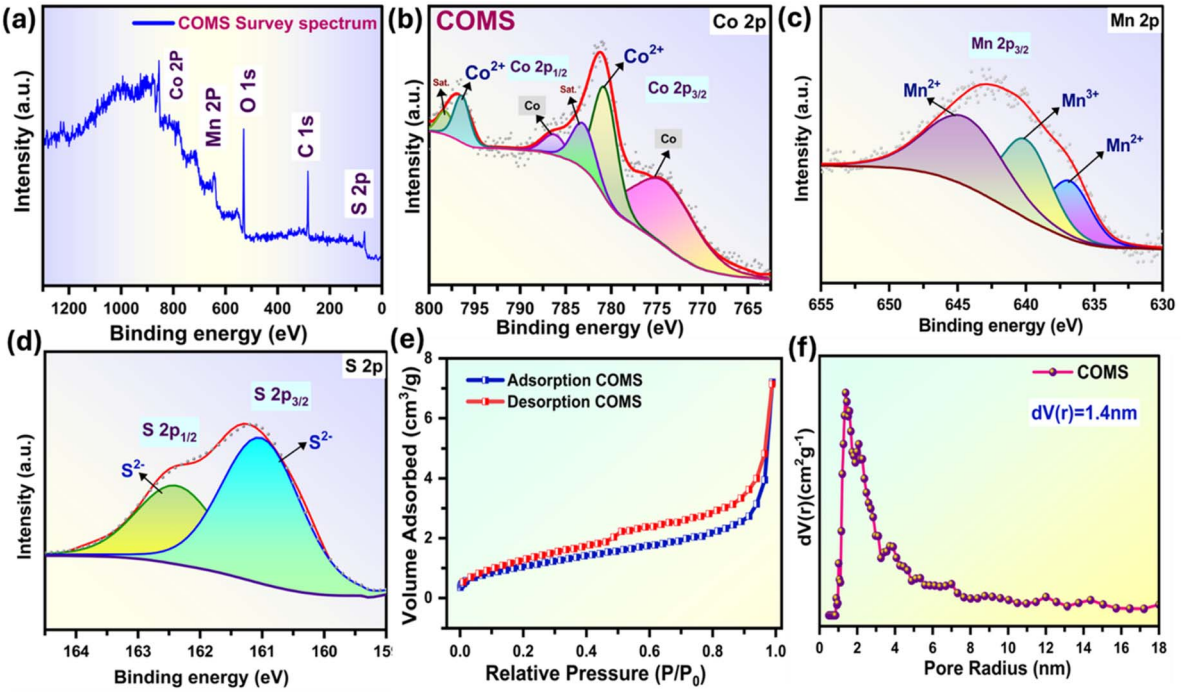

Fig. 4 (a–d) XPS spectra confirming the presence of Co, Mn, and S in COMS NSs on NF. (e) N_2 adsorption–desorption isotherm with a higher BET surface area. (f) BJH pore size distribution showing mesopores centered around 1.4 nm.

valence state.[48] This mixed valency is crucial, as it ultimately enhances and contributes to the superior catalytic performance in the HER and OER. Fig. 4d demonstrates the S 2p core level spectrum, with peaks at 161 eV and 162.4 eV consistent with S $2p_{3/2}$ and S $2p_{1/2}$, which is well associated with the divalent sulfide (S^{2-}) oxidation state.[49] Altogether, the phase integrity of the COMS NSs was validated.

The surface properties of the COMS NSs were evaluated using N_2 adsorption–desorption isotherms (Fig. 4e). The isotherm displays a typical type IV behaviour with a distinct H3-type hysteresis loop, denoting the presence of slit-like mesopores generated by the stacking of nanosheets.[50,51] The calculated BET surface area is 9.8 $m^2\ g^{-1}$, which directly correlates with the ultrathin, wrinkled morphology detected in the TEM images. Such a high surface area provides abundant active sites, facilitating improved contact between the electrode–electrolyte interface, which is beneficial for electrochemical water splitting.[52,53] The corresponding BJH pore size distribution (Fig. 4f) reveals a sharp peak at approximately 1.4 nm, suggesting dominant mesoporosity. These narrow mesopores not only aid in rapid electrolyte diffusion, but they also prevent bubble trapping, a common issue during gas evolution reactions.[54] Together, these characteristics confirm that the synthesized COMS NSs are structurally optimised for high electrocatalytic performance in water-splitting applications, validating the morphological and electronic design strategy.

To evaluate the electrocatalytic activity of the COMS NS electrocatalyst, the HER and OER performances were systematically examined in 1 M KOH electrolyte using a three-electrode configuration. Fig. 5a reveals the linear sweep voltammetry (LSV) curves of the COMS NSs and Pt/C for the HER, where the catalyst delivers a low overpotential of 197 mV and 29 mV to attain 10 mA cm^{-2} current density, suggesting remarkable catalytic activity. The corresponding Tafel slope in Fig. 5b were calculated to be 154 mV dec^{-1} for COMS NSs and 44 mV dec^{-1} for Pt/C, indicating the rate-limiting step. This moderately sloped region suggests efficient electron transfer and satisfactory conductivity across the electrocatalyst–electrolyte interface. In alkaline water electrolysis, the HER mechanism proceeds through water molecule dissociation rather than direct proton reduction.[55] The HER involves a two-electron process governed by the following plausible sequential steps:

(i) Volmer step – water dissociation and H adsorption*

The HER begins with the electrochemical dissociation of water at the catalyst surface. Water molecules then interact with the active sites of Co and Mn on COMS NSs and an electron, leading to the formation of adsorbed hydrogen (H_{ads} or H*) and OH^- (eqn (5)):

$$H_2O \rightarrow H_{ads} + OH^- - e^- \quad (5)$$

(ii) Heyrovsky step – electrochemical desorption

The adsorbed hydrogen reacts with another water molecule to produce molecular hydrogen (H_2), thereby releasing OH^- (eqn (6)):

$$H_2O + H_{ads} \rightarrow H_2 + OH^- - e^- \quad (6)$$

(iii) Tafel step – chemical recombination

Alternatively, when two H* species accumulate at neighbouring active sites, they can directly recombine to evolve hydrogen (eqn (7)):

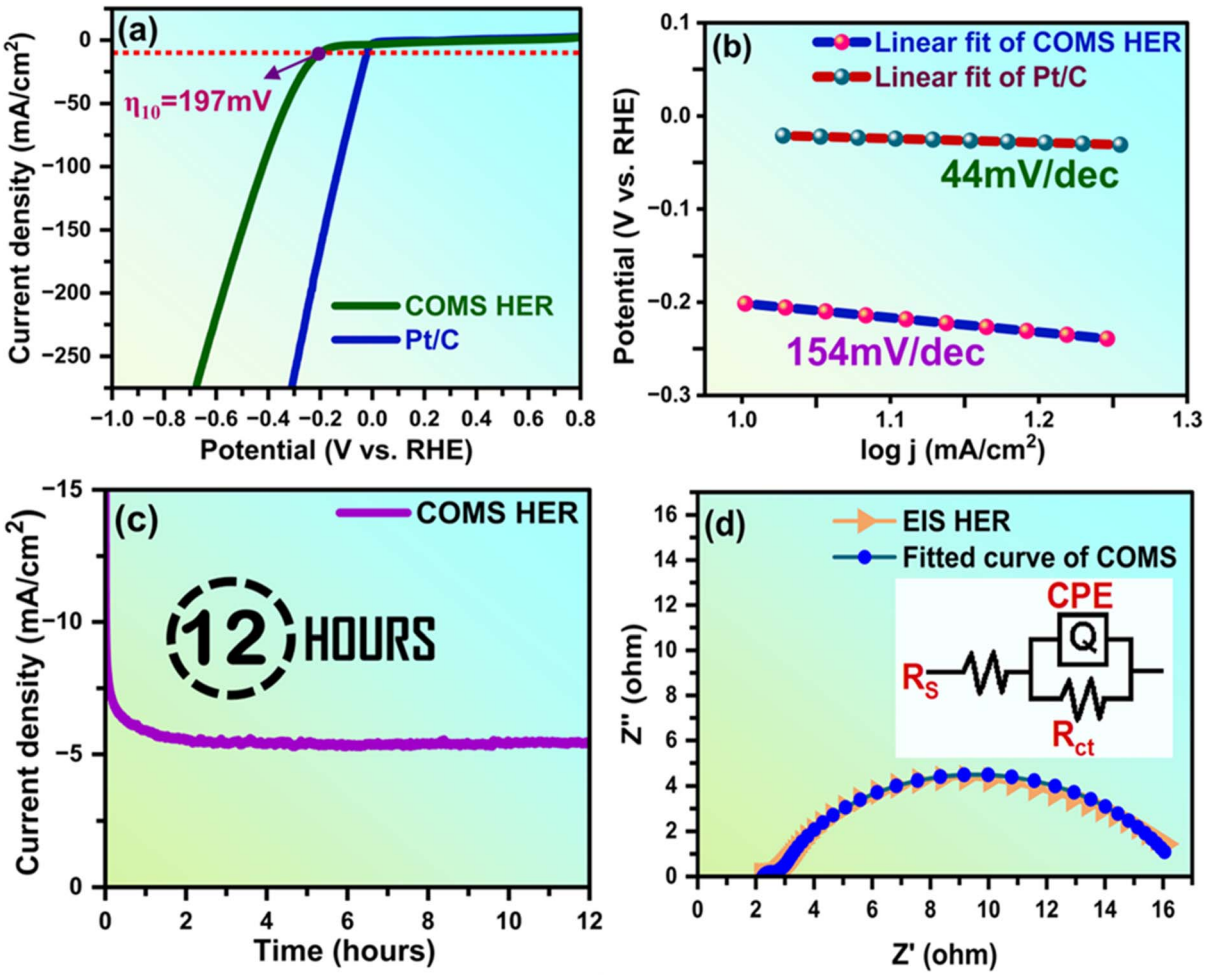

Fig. 5 Electrochemical measurements of COMS NSs: (a) HER polarization curve in 1 M KOH, (b) Tafel plot, (c) chronoamperometric HER stability, and (d) Nyquist plot with its equivalent circuit at HER potential.

$$H_{ads} + H_{ads} \rightarrow H_2 \quad (7)$$

This path is dominant when the catalyst surface achieves high H* coverage, which is supported by the large surface area and exposed active sites of the COMS NSs. The stability of COMS for the HER was verified through chronoamperometric analysis (Fig. 5c), which demonstrated satisfactory stability over 12 h, emphasizing its resilience during continuous hydrogen evolution.

EIS was performed to analyse the charge transfer kinetics of the obtained electrocatalyst. The Nyquist plot at an applied HER potential between the 100 kHz and 10 mHz frequency range is shown in Fig. 5d. Using the Randles equivalent circuit, the lowest solution resistance (R_s) of 2 Ω and a charge transfer resistance (R_{ct}) of 14 Ω was observed.

In the OER regime (Fig. 6a), the COMS NSs deliver an overpotential of 270 mV to attain 10 mA cm^{-2} current density, whereas RuO_2 obtained an overpotential of 270 mV. Also, from the LSV polarization curve, the Tafel slope value was found to be 177 mV dec^{-1} and 100 mV dec^{-1} for COMS NSs and RuO_2 (Fig. 6b), respectively, indicating favourable reaction kinetics and efficient oxygen intermediate formation (*O, *OH, *OOH). The OER catalytic process involves the adsorption and transformation of OH^- ions at the active sites of the COMS NSs.[55] The presumable mechanism proceeds *via* four electron processes *via* the following steps (X–COMS electrocatalyst): first step (eqn (8)) proceeds with the generation of the X–OH intermediate; the second step (eqn (9)) involves the continual interaction of X-OH^- with OH^- and releases a water molecule and an electron; the third step (eqn (10)) involves two discrete paths, thus leading to the existence of an O_2 molecule; the fourth step (eqn (11)) comprises the merging of a metal oxide and hydroxide to form metal oxyhydroxide; and finally, by utilizing proton-coupled electron transfer during oxidation, there exists O_2 and metal active sites (eqn (12)).

$$X + OH^- - e^- \rightarrow X\text{–}OH \quad (8)$$

$$X\text{–}OH^- + OH^- - e^- \rightarrow H_2O + X\text{–}O \quad (9)$$

$$X\text{–}O + X\text{–}O \rightarrow X + X + O_2 \quad (10)$$

$$X\text{–}O + OH^- - e^- \rightarrow X\text{–}OOH \quad (11)$$

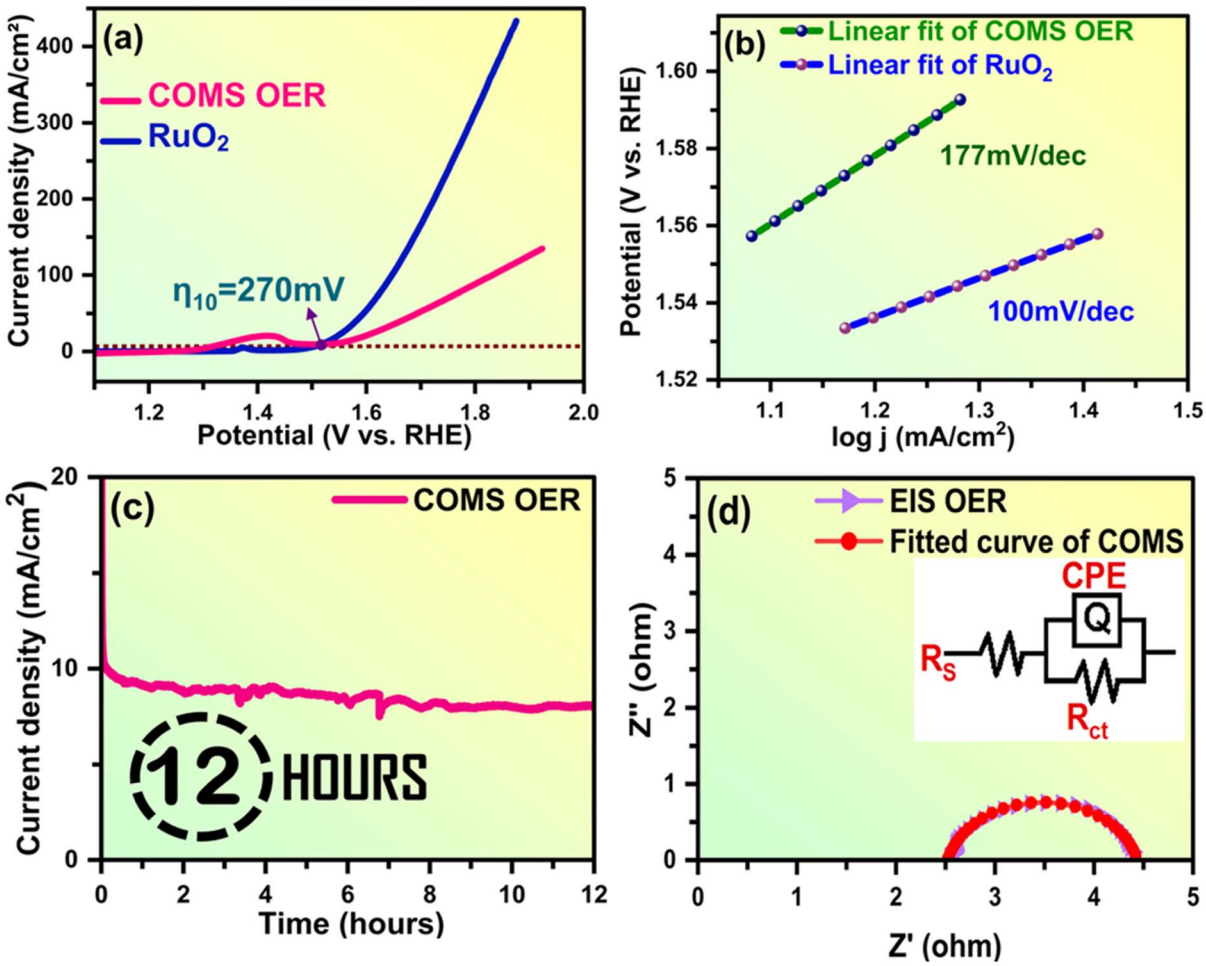

Fig. 6 Electrochemical measurements of COMS NSs: (a) OER polarization curve in 1 M KOH, (b) Tafel plot, (c) chronoamperometric OER stability, and (d) Nyquist plot with its equivalent circuit at OER potential.

$$X\text{–}OOH + OH^- - e^- \rightarrow O_2 + H_2O + X \quad (12)$$

Because of the presence of several intermediates, it is often difficult to identify the rate-determining steps and to understand the OER kinetics. The chronoamperometric stability (Fig. 6c) over 12 h shows a nearly steady current response, confirming the robust endurance under anodic bias. The electrocatalytic activity was also assessed by the ECSA by measuring the specific double-layer capacitance (C_{dl}) of the COMS NSs. From Fig. S1, the C_{dl} of COMS NSs was 5.55 mF cm^{-2}. It can be inferred that the attained electrocatalyst displays a larger ECSA (138 cm^2), which suggests it could expose more active sites for the HER and OER. The Nyquist plot shown in Fig. 6d displays the lowest solution resistance (R_s) of 2.6 Ω and a charge transfer resistance (R_{ct}) of 2.1 Ω, as determined using the Randles equivalent circuit.

Encouraged by the impressive HER and OER activities, the COMS NS electrocatalysts were further evaluated for overall water splitting in 1 M KOH using a two-electrode configuration. As shown in Fig. 7a, the system required only 1.54 V to achieve a current density of 10 mA cm^{-2}, and outperformed several reported catalysts (Table S1). The inset photograph confirmed the practical deployment of COMS NS//COMS NS electrodes in overall water splitting. Notably, the system maintained excellent durability over 300 h of continuous electrolysis with minimal variation in cell voltage (Fig. 7b). After 300 h of prolonged operation, XRD and HR-SEM post-analyses were performed. It was observed that the structure (inset, Fig. 7b) and the morphology of both the cathode and anode remained unchanged, indicating excellent stability (Fig. S2). Additionally, as demonstrated in Fig. 7a, there was only a slight increase in the overall cell potential from 1.54 V to 1.61 V compared to the prior 300 h of long-term stability.

3.1. Theoretical study

This theoretical study attempts to explain the significance of COMS NSs in the process of electrocatalytic water splitting. To interpret the theoretical outcomes of COMS NSs, DFT calculations were performed. The crystal structure of COMS consists of 16 cobalt (Co), 16 manganese (Mn), and 32 sulfur (S) atoms. The optimized geometry of the COMS monolayer is depicted in Fig. 8a and b, with top and side views affirming a stable configuration. The hexagonal lattice shows equilibrium lattice constants of a = 3.64 Å and b = 3.15 Å with Co–S and Mn–S bond lengths corresponding to 2.06 and 2.23 Å, respectively, thereby confirming the robustness of the metal–sulfur coordination.

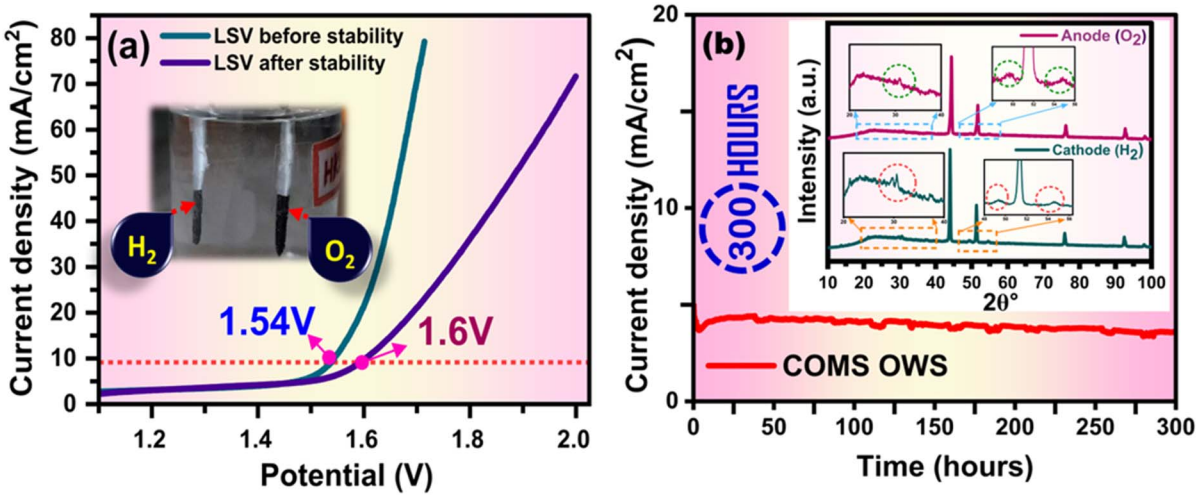

Fig. 7 Two electrode measurements of the COMS NSs: (a) LSV polarization curve of the obtained electrocatalyst before and after stability (inset: image of H_2 and O_2 evolution); and (b) long-term stability for 300 hours using chronoamperometry (inset: after stability XRD of the COMS//COMS electrocatalyst).

Fig. 8c displays the electronic band structure of the COMS NSs, revealing a zero bandgap that signifies the metallic behaviour. The existence of metallic behaviour effectively improves the catalytic performance of the resultant electrocatalyst,[56] thus facilitating the rapid charge transport to active sites in the HER and OER. Additionally, the total density of states (TDOS) and projected density of states (PDOS) further support these findings and are displayed in Fig. 8d. The notable contributions from the Co 3d and Mn 3d orbitals at the Fermi level indicate a high density of electronic states, resulting in superior conductivity and effective electrocatalytic performance.[57] Collectively, the theoretical findings offer a plausible argument for the effective electrocatalytic performance of the COMS NSs, and highlight the potential of this class of materials to act as bifunctional electrocatalysts for overall water splitting.

COMS NSs exhibit superior bifunctional activity due to many synergistic factors, including the mixed valence states of Co and Mn in the sulfur-expanded lattice, the high porosity and surface

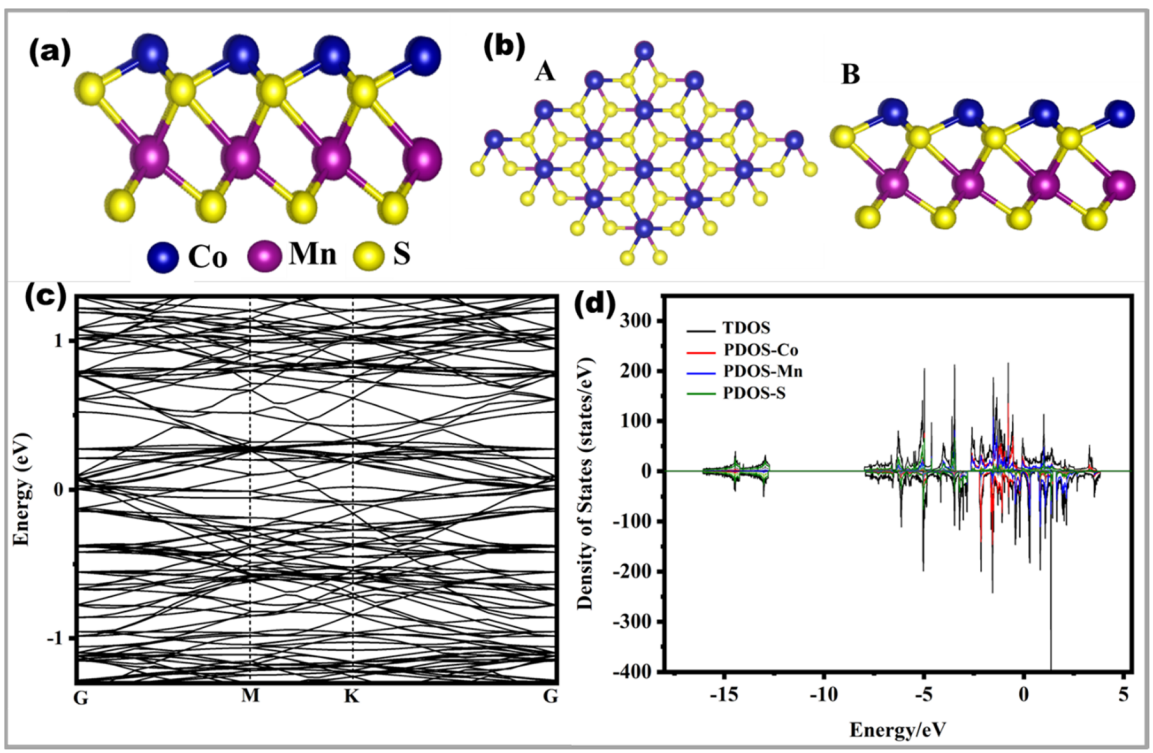

Fig. 8 (a) Optimized geometry of the COMS structure. (b) COMS structure ((A) top view; (B) side view). (c) Electronic band structure. (d) Total and projected density of states of the COMS electrocatalyst.

area, which lead to efficient ion/electron transport pathways in the nanosheet-like array morphology, and improved electrolyte contact and reduced interfacial resistance. These features render binder-free COMS NSs a highly active and stable bifunctional electrocatalyst.

4 Conclusions

A cobalt manganese sulfide nanosheet was grown *in situ* on nickel foam *via* a simple hydrothermal method. As a result of the combination of activity, stability, and cost-effectiveness, COMS NSs are promising bifunctional electrocatalysts for alkaline overall water splitting. The synthesized binder-free COMS NSs performed well for the HER and OER, with a low overpotential of 197 mV and 270 mV, respectively, to reach 10 mA cm^{-2} current density. Interestingly, it exhibited a low overall cell potential of 1.54 V, with a prolonged stability of 300 h. The nanosheet-like morphology, higher surface area, mesoporous structure, and multiple valence states of metal atoms are the reasons behind the improved performance of the COMS NS electrocatalyst. Moreover, the experimental findings are well supported by the theoretical observations and strengthen the role of COMS NSs in electrocatalysis. Thus, the developed electrocatalyst could serve as a viable replacement for noble metal-based precious electrocatalysts as a bifunctional electrocatalyst, provided it demonstrates practical viability.

Author contributions

H. S. performed the experimental work and drafted the manuscript. H. S. acknowledges A. M. for designing the study. A. K. and S. L. are thankfully acknowledged for their contributions to the DFT calculations and theoretical analyses. P. K. and J. M. contributed to the critical revision and refinement of the manuscript.

Conflicts of interest

The authors declare no conflicts of interest.

Data availability

The data are available upon request from the authors.

Supplementary information (SI): ECSA analysis, post-stability HR-SEM, and a comparison table of COMS NSs with the literature and BET experimental conditions. See DOI: https://doi.org/10.1039/d5se01288k.

Acknowledgements

The authors acknowledge the financial support from the Department of Physics and Nanotechnology, SRM Institute of Science and Technology, Kattankulathur, Chennai. The authors acknowledge the NRC for the XRD, FT-IR, and XPS facilities, and SCIF for the HR-SEM, HR-TEM, and BET facilities. The authors would also like to thank Dr Kumaran Vediappan, Department of Chemistry, SRM Institute of Science and Technology, Kattankulathur, Chennai, for his support with electrochemical measurements.

References

1 S. Swain, B. Sirichandana, P. Bhol, K. S. Anantharaju and G. Hegde, *Sustainable Energy Fuels*, 2025, **9**, 2870–2899.
2 F. ElBachraoui, D. Aymé-Perrot and H. H. Girault, *Research*, 2025, **8**, 0788.
3 A. Patel, S. K. Patel, R. S. Singh and R. P. Patel, *Discover Nano*, 2024, **19**, 1–42.
4 W. H. Huang, X. M. Li, X. F. Yang, H. B. Zhang, F. Wang and J. Zhang, *Chem. Commun.*, 2021, **57**, 4847–4850.
5 S. C. Jesudass, S. Surendran, D. J. Moon, S. Shanmugapriya, J. Y. Kim, G. Janani, K. Veeramani, S. Mahadik, I. G. Kim, P. Jung, G. Kwon, K. Jin, J. K. Kim, K. Hong, Y. Il Park, T.-H. Kim, J. Heo and U. Sim, *J. Colloid Interface Sci.*, 2024, **663**, 566–576.
6 F. Ren, J. Xu and L. Feng, *Nano Res.*, 2024, **17**, 3785–3793.
7 S. Kartigueyane, S. P. Kumar Arunachala Kumar, M. S. AlSalhi, S. P. Rajendra, I. In, S. J. Lee, C. Yan and S. Angaiah, *ACS Appl. Energy Mater.*, 2025, **8**, 5004–5016.
8 L. Zhao, S. Liu, L. Wei, H. He, B. Jiang, Z. Zhan, J. Wang, X. Li and W. Gou, *Catal. Lett.*, 2024, **154**, 5294–5302.
9 V. Jayaraman, G. Jang, G. H. Noh, M. Murmu and D. H. Kim, *J. Mater. Chem. A*, 2024, **12**, 17663–17675.
10 X. Li, Y. Huang, D. Chu, K. Kajiyoshi, Y. Liu, Y. Zhao, Q. Chen, R. Liu, L. Cao, L. Feng and J. Huang, *ACS Appl. Nano Mater.*, 2025, **8**, 7026–7038.
11 Y. Liao, Z. He, W. Hong, Q. Dong, X. Gou and R. Li, *New J. Chem.*, 2025, **49**, 7164–7170.
12 Y. Luan, X. Yan, C. Ji, C. Lv, D. Lan, S. Zhang, J. Sun, D. Li and G. Wu, *J. Mater. Sci. Technol.*, 2025, **228**, 279–286.
13 X. Liao, Z. Huang, W. Zhang, Y. Meng, L. Yang and Q. Gao, *J. Colloid Interface Sci.*, 2024, **674**, 1048–1057.
14 H. S. Han, F. Yi, S. Choi, J. Kim, J. Kwon, K. Park and T. Song, *J. Alloys Compd.*, 2020, **846**, 156350.
15 D. C. Cha, J. H. Seok, S. C. Cho, M. Singh, T. I. Singh, S. U. Lee and S. Lee, *Small*, 2025, 2500334.
16 L. Yang and L. Li, *J. Phys. Chem. Solids*, 2025, **207**, 112926.
17 X. Liu, T. Huang, J. Xiao, N. Liu, Z. Yu, L. Zhang and G. Xu, *ACS Appl. Nano Mater.*, 2025, **8**, 13139–13148.
18 A. E. Fetohi, D. Z. Khater, R. S. Amin and K. M. El-Khatib, *J. Phys. Chem. Solids*, 2025, **207**, 112906.
19 M. Abdul, M. Zhang, T. Ma, N. H. Alotaibi, S. Mohammad and Y. S. Luo, *Nanoscale Adv.*, 2025, **7**, 433–447.
20 R. C. Gotame, Y. R. Poudel, G. Ghimire, R. Pathak, J. W. Elam, J. Watt, W. Kuo and W. Li, *ACS Electrochem.*, 2025, **1**, 1125–1140.
21 A. Bist, J. Gautam, S. Y. Lee and S. J. Park, *Small*, 2025, 2505022.
22 A. K. Samal, P. Bhol, S. Swain, T. Jaikumar, S. A. Patil and P. K. Misra, *ACS Appl. Nano Mater.*, 2025, **8**, 14328–14341.
23 A. Kareem, E. Jose, K. Thenmozhi and S. Senthilkumar, *ACS Appl. Nano Mater.*, 2025, **8**, 8424–8432.
24 A. K. Nayak and D. Pradhan, *ACS Appl. Energy Mater.*, 2025, **8**, 2088–2102.

25 H. He, D. Zhu, C. Huang, G. Chang, Y. Qian, M. Ran, A. Hu, X. Chen and Q. Tang, *ACS Appl. Mater. Interfaces*, 2025, **17**, 29535–29545.
26 S. Swathi, R. Yuvakkumar, G. Ravi, M. Thambidurai and D. Velauthapillai, *Carbon*, 2024, **229**, 119466.
27 K. C. Majhi and M. Yadav, *ACS Eng. Au*, 2023, **3**, 278–284.
28 A. P. Tiwari, K. Kim and S. Jeon, *Curr. Opin. Electrochem.*, 2022, **34**, 100982.
29 S. Qiang, Z. Li, S. He, H. Zhou, Y. Zhang, X. Cao, A. Yuan, J. Zou, J. Wu and Y. Qiao, *Nano Energy*, 2025, **134**, 110564.
30 S. Huang, S. Ma, L. Liu, Z. Jin, P. Gao, K. Peng, Y. Jiang, A. Naseri, Z. Hu and J. Zhang, *J. Colloid Interface Sci.*, 2023, **652**, 369–379.
31 P. P. Dhakal, U. N. Pan, D. R. Paudel, M. R. Kandel, N. H. Kim and J. H. Lee, *Mater. Today Nano*, 2022, **20**, 100272.
32 W. F. Chen, K. Sasaki, C. Ma, A. I. Frenkel, N. Marinkovic, J. T. Muckerman, Y. Zhu and R. R. Adzic, *Angew. Chem., Int. Ed.*, 2012, **51**, 6131–6135.
33 J. Xie, S. Li, X. Zhang, J. Zhang, R. Wang, H. Zhang, B. Pan and Y. Xie, *Chem. Sci.*, 2014, **5**, 4615–4620.
34 G. Kresse and J. Furthmüller, *Phys. Rev. B: Condens. Matter Mater. Phys.*, 1996, **54**, 11169–11186.
35 G. Kresse and J. Hafner, *Phys. Rev. B: Condens. Matter Mater. Phys.*, 1993, **47**, 558.
36 J. P. Perdew, K. Burke and M. Ernzerhof, *Phys. Rev. Lett.*, 1996, **77**, 3865.
37 S. Grimme, *J. Comput. Chem.*, 2006, **27**, 1787–1799.
38 S. Fazil, K. S. Ahmad, Z. Hussain and S. Sharif, *Research & Reviews: Journal of Material Sciences*, 2017, **5**, 166–174.
39 R. Vikkash, S. Muthukumaran and M. Rakchana, *J. Mater. Sci.: Mater. Electron.*, 2025, **36**, 1–21.
40 J. Wang, Z. Zhong, B. Chen, S. Luo, A. Xie and B. Yang, *Langmuir*, 2025, **41**, 23917–23931.
41 T. Wang, F. Chen, J. Wang, C. Wang, L. Kuai and B. Geng, *Chem. Commun.*, 2023, **59**, 298–301.
42 P. Wang, C. Yang, J. Yao, H. Li, Z. Hu and Z. Li, *Chem. Sci.*, 2025, **16**, 6583–6597.
43 S. Balasubramanyam, M. Shirazi, M. A. Bloodgood, L. Wu, M. A. Verheijen, V. Vandalon, W. M. M. Kessels, J. P. Hofmann and A. A. Bol, *Chem. Mater.*, 2019, **31**, 5104–5115.
44 Z. Xu, Z. Pang, S. Alshammari, X. Yan, H. K. Thabet, X. Jiang, Z. M. El-Bahy, X. Xu and L. Yu, *Chem. Eng. J.*, 2025, **522**, 166426.
45 B. Jiang, Y. Guo, F. Sun, S. Wang, Y. Kang, X. Xu, J. Zhao, J. You, M. Eguchi, Y. Yamauchi and H. Li, *ACS Nano*, 2023, **17**, 13017–13043.
46 J. C. da Cruz, R. M. e Silva, G. T. S. T. da Silva, L. H. Mascaro and C. Ribeiro, *Sustainable Energy Fuels*, 2024, **8**, 3104–3112.
47 J. Lu, Y. Zeng, X. Ma, H. Wang, L. Gao, H. Zhong and Q. Meng, *Polymers*, 2019, **11**, 828.
48 A. Thomas, A. Narayanan, S. M. Pillai, R. Bhar, M. Lastovich and B. Gwalani, *ACS Appl. Mater. Interfaces*, 2025, **17**, 16812–16824.
49 Q. Dong, Y. Sun, F. Wang, Z. Zhang and S. Min, *Sustainable Energy Fuels*, 2024, **8**, 4907–4913.
50 C. Schlumberger and M. Thommes, *Adv. Mater. Interfaces*, 2021, **8**, 2002181.
51 M. Thommes, K. Kaneko, A. V. Neimark, J. P. Olivier, F. Rodriguez-Reinoso, J. Rouquerol and K. S. W. Sing, *Pure Appl. Chem.*, 2015, **87**, 1051–1069.
52 J. Huang, Y. Jiang, T. An and M. Cao, *J. Mater. Chem. A*, 2020, **8**, 25465–25498.
53 M. Yang, C. H. Zhang, N. W. Li, D. Luan, L. Yu and X. W. Lou, *Adv. Sci.*, 2022, **9**, 2105135.
54 T. Kadyk, D. Bruce and M. Eikerling, *Sci. Rep.*, 2016, **6**, 1–14.
55 Y. Wang, F. Li, L. Zhao, Y. Wang, G. Yang, J. Tian, S. Heng, X. Sun, J. Zhao, M. Chen and Q. Chen, *Nanoscale*, 2025, **17**, 11101–11132.
56 H. Sharan, A. Kausalya, S. Lakshmipathi, J. Madhavan, P. Karthikesan and A. Mani, *ACS Appl. Energy Mater.*, 2025, **8**, 13752–13762.
57 H. Muhammad Naeem Ullah, N. Mushtaq, S. Ur Rehman, Z. Tariq, S. S. Ali, M. Tahir, C. Li, X. Zhang and J. Li, *J. Colloid Interface Sci.*, 2025, **678**, 1087–1095.